

Extended star-forming regions within galaxies in a dense proto-cluster core at $z = 2.53^\dagger$

Tomoko L. SUZUKI,^{1,2,*} Yosuke MINOWA,^{3,4} Yusei KOYAMA,^{3,4}
Tadayuki KODAMA,¹ Masao HAYASHI,² Rhythm SHIMAKAWA,³ Ichi TANAKA,³
and Ken-ichi TADAKI²

¹Astronomical Institute, Tohoku University, 6-3 Aramaki, Aoba-ku, Sendai, Miyagi 980-8578, Japan

²National Astronomical Observatory of Japan, 2-21-1 Osawa, Mitaka, Tokyo 181-8588, Japan

³Subaru Telescope, National Astronomical Observatory of Japan, National Institutes of Natural Sciences, 650 North A'ohoku Place, Hilo, HI 96720, USA

⁴Department of Astronomical Science, SOKENDAI (The Graduate University for Advanced Studies), 2-21-1 Osawa, Mitaka, Tokyo 181-8588, Japan

*E-mail: suzuki.tomoko@nao.ac.jp

[†]Based on data collected at Subaru Telescope, which is operated by the National Astronomical Observatory of Japan.

Received 2019 February 14; Accepted 2019 April 1

Abstract

At $z \sim 2$, star formation activity is thought to be high even in high-density environments such as galaxy clusters and proto-clusters. One of the critical but outstanding issues is if the structural growth of star-forming galaxies can differ depending on their surrounding environments. In order to investigate how galaxies grow their structures and what physical processes are involved in the evolution of galaxies, one requires spatially resolved images of not only stellar components but also star-forming regions within galaxies. We conducted (Adaptive Optics) AO-assisted imaging observations for star-forming galaxies in a dense proto-cluster core at $z = 2.53$ with IRCS and AO188 mounted on the Subaru Telescope. A combination of AO and narrow-band filters allows us to obtain resolved maps of H α -emitting regions with an angular resolution of $0''.1$ – $0''.2$, which corresponds to ~ 1 kpc at $z \sim 2.5$. Based on stacking analyses, we compare radial profiles of star-forming regions and stellar components and find that the star-forming region of a sub-sample with $\log(M_*/M_\odot) \sim 10$ – 11 is more extended than the stellar component, indicating the inside-out growth of the structure. This trend is similar to the one for star-forming galaxies in general fields at $z = 2$ – 2.5 obtained with the same observational technique. Our results suggest that the structural evolution of star-forming galaxies at $z = 2$ – 2.5 is mainly driven by internal secular processes irrespective of surrounding environments.

Key words: galaxies: evolution — galaxies: high-redshift — galaxies: star formation — galaxies: structure

1 Introduction

High-density environments at $z \gtrsim 2$, such as galaxy clusters and proto-clusters, are often associated with active star-forming galaxies (e.g., Venemans et al. 2007; Hayashi et al.

2012; Gobat et al. 2013; Koyama et al. 2013; Kato et al. 2016; Wang et al. 2016) as opposed to local galaxy clusters, which are dominated by passive elliptical galaxies. The environmental dependence of physical quantities of star-forming galaxies at $z \gtrsim 2$, such as star-forming activity,

gas metallicity, and morphology, has been investigated in many studies (see Overzier 2016 and reference therein) with the aim of understanding the early stage of the environmental effects on galaxy formation and evolution. However, the environmental dependence of structural growth of star-forming galaxies at high redshift has still not been investigated. Some studies on the rest-frame optical or rest-frame UV structures of star-forming galaxies in (proto-)cluster environments at $z > 1$ have already been carried out (Peter et al. 2007; Overzier et al. 2008; Wang et al. 2016; Allen et al. 2017; Kubo et al. 2017; Shimakawa et al. 2018; Matharu et al. 2019; Socolovsky et al. 2019). However, it is yet required to trace the structures of star-forming regions as well as underlying stars directly (e.g., Nelson et al. 2016b; Tacchella et al. 2018; Belfiore et al. 2018; Ellison et al. 2018) to investigate how star-forming galaxies build up their structures and what physical processes are involved in their evolution.

The structural growth of star-forming galaxies in general fields is investigated with the redshift evolution of stellar size (e.g., Trujillo et al. 2006; Franx et al. 2008; van der Wel et al. 2014; Shibuya et al. 2015). A positive correlation between stellar mass and size as well as a slow redshift evolution of size indicate that galaxies increase their stellar masses generally by adding new stars to the outer regions, i.e., inside-out growth (e.g., Trujillo et al. 2006). The structural growth is also investigated by directly tracing ongoing star formation within galaxies (e.g., Nelson et al. 2016b; Tacchella et al. 2018; Belfiore et al. 2018; Ellison et al. 2018). In Nelson et al. (2016b), it was shown that star-forming galaxies at $z \sim 1$ grow their structures from inside to outside by mapping the spatial distribution of H α -emitting region.

From theoretical studies, a “compaction” event is suggested as an evolutionary path of galaxies especially at higher redshift, where galaxies are more gas-rich (Zolotov et al. 2015; Tacchella et al. 2016). The compaction event can be triggered by gas-rich major mergers (e.g., Mihos & Hernquist 1996) or violent disk instabilities of a gas-rich disk (e.g., Noguchi 1999), which drives molecular gas in the disk toward the center and induces starburst (Dekel & Burkert 2014). The star-forming region is centrally concentrated in the compaction event, and thus, the spatial distribution of the star-forming region is expected to become different from that of the inside-out growth.

The relative contribution among these physical processes may depend on the environments in which galaxies reside. The gas inflow process to make gravitationally unstable disks or the frequency of major mergers possibly depend on the surrounding environments. Galaxies in cluster environments reside in more massive dark matter halos than their field counterparts. Such cluster galaxies tend to be fed by

more intense cold gas inflow from the outside until their dark matter halo masses exceed a critical mass where the mode of gas accretion would change as predicted by cosmological simulations (e.g., Kereš et al. 2005, 2009; Dekel & Birnboim 2006). In high-density environments, the frequency of galaxy mergers can be high, as reported in Lotz et al. (2013) and Hine et al. (2016). Additionally, galaxies in cluster environments can be affected by characteristic physical processes in cluster regions. Ram pressure stripping (Gunn & Gott 1972) would be effective at least in local galaxy clusters and remove the gas associated with the outer part of galaxies. Galaxies in local clusters tend to have centrally concentrated star-forming regions [e.g., Koopmann and Kenney (2004) and Schaefer et al. (2019) for local group-class environments]. When a dominant physical process is different depending on the environments, such a difference is expected to be reflected in the internal structures of star-forming regions.

Near-infrared (NIR) integral-field-unit (IFU) observations with the Adaptive Optics (AO) system are commonly conducted to obtain spatially resolved star-forming regions for galaxies at $z \gtrsim 1$ (e.g., Law et al. 2007, 2009; Förster Schreiber et al. 2009, 2018; Swinbank et al. 2012). AO-assisted high resolution imaging with narrow-band (NB) filters also enables us to trace line-emitting star-forming regions within galaxies in a particular redshift slice. The major limitation of the AO-assisted observations is a narrow field of view (FoV). However, the observational efficiency can be high in the case of dense cluster cores at high redshifts, as many galaxies can fall within a single FoV and all of them can be spatially resolved at the same time. Moreover, by using the H α emission line as a tracer of star-forming regions, one can trace even relatively dusty star-forming regions which tend to be missed by the rest-frame UV observations (e.g., Wuyts et al. 2013; Tadaki et al. 2014).

We have been conducting K' -band and NB imaging observations for star-forming galaxies at $z = 2$ – 2.5 with the Infrared Camera and Spectrograph (IRCS; Tokunaga et al. 1998; Kobayashi et al. 2000) and AO system (AO188; Hayano et al. 2008, 2010) on the Subaru Telescope (co-PIs: Y. Minowa and Y. Koyama). This project aims to resolve strong emission lines as well as stellar continua for star-forming galaxies at $z = 2$ – 2.5 spatially across environments, and finally to reveal the build-up of the stellar structures of galaxies and its environmental dependence. The targets of this project are H α -selected star-forming galaxies at $z = 2$ – 2.5 , which are originally obtained by NB imaging surveys, namely Mahalo-Subaru (Mapping H α and Lines of Oxygen with Subaru; Kodama et al. 2013) and HiZELS [the High-redshift(Z) Emission Line Survey; Best et al. 2013; Sobral et al. 2013]. The targets consist of galaxies in general

fields, such as the Cosmic Evolution Survey (COSMOS) field and the Ultra Deep Survey (UDS) field (Sobral et al. 2013; Tadaki et al. 2013), and also in proto-cluster fields (Hayashi et al. 2012; Koyama et al. 2013). Because the same NB filters which were used to detect the $H\alpha$ emitters are installed on IRCS, we can trace the $H\alpha$ -emitting region within the $H\alpha$ emitters with an angular resolution of $0''.1$ – $0''.2$ by AO-assisted NB imaging observations. This angular resolution scale corresponds to ~ 1 kpc at $z = 2$ – 2.5 . By targeting the NB-selected galaxies, the emission line fluxes of which are already known, we can achieve a high observational efficiency. As for the field galaxies, 20 $H\alpha$ emitters in the COSMOS and UDS fields were observed. The sample covers a stellar mass range of $\log(M_*/M_\odot) \sim 9$ – 11 . Observational results for the $H\alpha$ emitters in the general fields are reported in a different paper (Minowa et al. 2019). Here we show results for the $H\alpha$ emitters in a proto-cluster environment at $z = 2.53$, and compare the results in the proto-cluster and general fields.

The paper is organized as follows: In section 2, we describe the target proto-cluster to be studied in this paper, followed by the details of the observations with Subaru/IRCS + AO188. In section 3, we explain our data analyses to obtain spatially resolved stellar continuum maps and emission line maps from the images. In section 4, we show our results based on the stacking analyses focusing on any environmental dependence in the spatial extent of star-forming regions within the galaxies at $z = 2$ – 2.5 . We summarize this study in section 5.

Throughout this paper, we assume the cosmological parameters of $\Omega_m = 0.3$, $\Omega_\Lambda = 0.7$, and $H_0 = 70 \text{ km s}^{-1} \text{ Mpc}^{-1}$. All the magnitudes are given in an AB system, and we use the Chabrier initial mass function (IMF; Chabrier 2003), unless otherwise noted.

2 Target field and observation

2.1 A dense proto-cluster core at $z = 2.53$

Our target field is a proto-cluster, USS 1558-003 (hereafter USS1558), which is associated with a radio galaxy at $z = 2.53$ (Kajisawa et al. 2006). NB imaging observations for this proto-cluster were conducted with Subaru/Multi-Object InfraRed Camera and Spectrograph (MOIRCS; Ichikawa et al. 2006). So far, 107 $H\alpha$ emitters are identified in this proto-cluster based on color–color selections (Hayashi et al. 2012, 2016; Shimakawa et al. 2018).

The stellar mass–star formation rate (SFR) relation of the $H\alpha$ emitters in USS1558 is shown in figure 1. Here stellar masses were estimated from spectral energy distribution (SED) fitting using seven broad-band photometries, namely, B , r' , z' , J , H , $F160W$, and K_s , by Shimakawa et al.

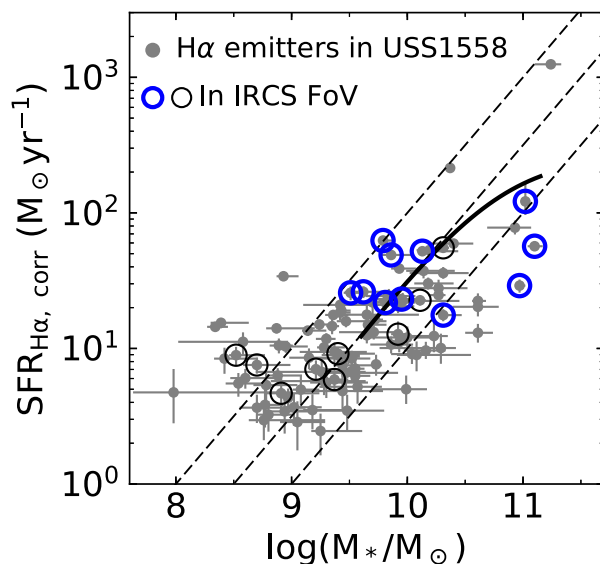


Fig. 1. Stellar mass–SFR relation for the $H\alpha$ emitters in USS1558 (Hayashi et al. 2012, 2016; Shimakawa et al. 2018). Open circles show the $H\alpha$ emitters covered in the IRCS FoV. The thick blue circles correspond to the $H\alpha$ emitters analyzed in this study (subsection 2.2). Dotted lines represent constant sSFRs (SFR/M_*), namely, $\log(\text{sSFR}[\text{yr}^{-1}]) = -8.0$, -8.5 , and -9.0 . The thick solid line shows the star-forming main sequence at $z = 2.53$ from Tomczak et al. (2016). Our IRCS + AO188 targets are located around the “main sequence” of star-forming galaxies at this epoch. (Color online)

(2018). Because we use a different method to estimate dust extinction for $H\alpha$ ($A_{H\alpha}$) from previous studies (Hayashi et al. 2012, 2016; Shimakawa et al. 2018), we re-calculate SFRs of the $H\alpha$ emitters. SFRs are calculated using the relation between SFRs and $H\alpha$ luminosities from Kennicutt (1998) considering the difference between Chabrier and Salpeter IMF (Salpeter 1955). When calculating the $H\alpha$ luminosity of the individual emitters from the MOIRCS NB imaging data, we subtract a $[\text{N II}]$ flux from a total NB flux by estimating a $[\text{N II}]/H\alpha$ ratio from an empirical relation between $[\text{N II}]/H\alpha$ and the equivalent-width (EW) of $H\alpha + [\text{N II}]$ (Sobral et al. 2012). $A_{H\alpha}$ is estimated using an empirical relation among $A_{H\alpha}$, EW of $H\alpha$ in the rest-frame, and a ratio between observed SFRs estimated from $H\alpha$ and UV established by Koyama et al. (2015). More details of this method of estimating $A_{H\alpha}$ is mentioned in subsection 4.1. The $H\alpha$ emitters in USS1558 show a positive correlation between stellar masses and SFRs, known as the “main sequence” of star-forming galaxies (e.g., Noeske et al. 2007; Daddi et al. 2007; Kashino et al. 2013; Tomczak et al. 2016), as already reported in previous studies (Hayashi et al. 2012, 2016; Shimakawa et al. 2018).

The spatial distribution of the $H\alpha$ emitters in USS1558 is characterized by several groups of $H\alpha$ emitters. The densest group is located at 1.5 Mpc away from the radio galaxy (figure 5 in Hayashi et al. 2012), and its local surface

Table 1. Summary of the obtained data in USS1558 with IRCS + AO188.*

Band	Dates (UT)	Exposure time (hr)	FWHM ($''$)	$m_{\text{lim}, 3\sigma}$ (mag)	AO mode
K'	2013 May 7	2.2	0.25	25.55	LGS
NB2315	2014 May 17, 18, 22	7.4	0.17	24.09	LGS

*The limiting magnitude is obtained with a $0''.5$ diameter aperture.

density is 30 times higher than that in the general field (Hayashi et al. 2012). We observed this densest group with Subaru/IRCS + AO188. In total, 20 $\text{H}\alpha$ emitters are covered in the IRCS FoV ($53 \times 53 \text{ arcsec}^2$).

2.2 Observation with Subaru/IRCS + AO188

We conducted K' -band and NB imaging observations for USS1558 with Subaru/IRCS + AO188 in 2013 May and 2014 May (S13A-059 and S14A-019; PI: Y. Koyama). We used the NB2315 filter ($\lambda_c = 2.314 \mu\text{m}$, full-width at half-maximum = $0.03 \mu\text{m}$) to catch the $\text{H}\alpha$ emission line from galaxies at $z = 2.53$. The observations were conducted using the laser guide star (LGS) mode (Minowa et al. 2012) with a tip-tilt guide star of $R = 14.9$ mag. The on-source exposure time of each frame was 50 and 200 s for K' -band and NB2315, respectively.

Data reduction was conducted using the IRCS imaging pipeline software, which was originally developed by Minowa et al. (2005) and updated with python scripts by Y. Minowa. The pipeline follows a standard reduction procedure: flat-fielding with sky flat frames, distortion correction, sky subtraction, and combining the frames. The reduction procedure was repeated twice to make an accurate bright object mask for sky flat frames. When combining the frames, we excluded the frames with an extremely large full-width at half-maximum (FWHM). The total exposure time of the final K' -band and NB2315 images is 2.2 and 7.4 hours, respectively. The 3σ limiting magnitude of K' -band and NB2315 is 25.55 and 24.09 mag with a $0''.5$ diameter aperture. The achieved point spread function (PSF) size is $0''.25$ and $0''.17$ in FWHM for the K' -band and NB2315 images (table 1).

Whereas 20 $\text{H}\alpha$ emitters are covered by the IRCS FoV, the $\text{H}\alpha$ emitters with $\log(M_*/M_\odot) < 9.5$ are barely detected in both K' -band and NB images. Considering the signal-to-noise ratios (S/N) of the data, we decided to use only relatively massive $\text{H}\alpha$ emitters with $\log(M_*/M_\odot) \geq 9.5$. We also exclude three $\text{H}\alpha$ emitters neighboring bright objects. In the following sections, we analyze the remaining 11 $\text{H}\alpha$ emitters. The locus of the 11 $\text{H}\alpha$ emitters on the stellar mass–SFR diagram is shown in figure 1, demonstrating that our targets are around the “main sequence” in USS1558. We note that our IRCS targets with $\log(M_*/M_\odot) = 9.5$ –10 are at an upper edge of the main sequence. This is related

to an observational result that the $\text{H}\alpha$ emitters in the dense groups in USS1558 tend to have higher SFRs than those in less-dense regions with similar stellar masses (Shimakawa et al. 2018).

3 Data analysis

3.1 PSF matching

Because the PSF size of the NB image is smaller than that of the K' -band image (table 1), we smooth the NB image so that we can subtract the K' -band image from the NB image to obtain continuum-subtracted emission line maps. However, comparing the shapes of several stars in the NB image, their shapes are slightly elongated in different directions probably depending on their positions relative to the LGS. We need to conduct the PSF matching for the individual $\text{H}\alpha$ emitters according to their position in the FoV.

We fit the K' -band and NB images of the seven stars with a Moffat function using GALFIT (Peng et al. 2010) to make model PSF images. Then, we create PSF convolution kernels using the model PSF images of the two bands and the PSFMATCH task in the IRAF environment.¹ The NB images of the individual $\text{H}\alpha$ emitters are smoothed with PSFMATCH by convolving the kernel created from the model PSF images of the closest star. Because some of the $\text{H}\alpha$ emitters at the center of the image have no suitable star, we create the model PSF images of K' -band and NB for such $\text{H}\alpha$ emitters by taking an average of the model PSF profiles of the seven stars.

The PSF shapes of the seven stars in the K' -band image are almost independent from its position in the FoV, and thus, the PSF shapes of the convolved NB images are thought to be the same among all the $\text{H}\alpha$ emitters. After the PSF matching, the FWHM of the K' -band and NB image is $0''.25$, corresponding to 2 kpc at $z = 2.53$.

By subtracting the K' -band image from the PSF-matched NB image for the individual $\text{H}\alpha$ emitters, we obtain their continuum-subtracted $\text{H}\alpha + [\text{N II}]$ emission line images. The K' -band image itself corresponds to the underlying stellar continuum because NB2315 has little overlap with the K' -band in wavelength. Figure 2 shows the K' -band and NB2315– K' images taken with Subaru/IRCS + AO188 and the I_{F814W} -band images taken with the Hubble Space

¹ (<http://iraf.noao.edu/>).

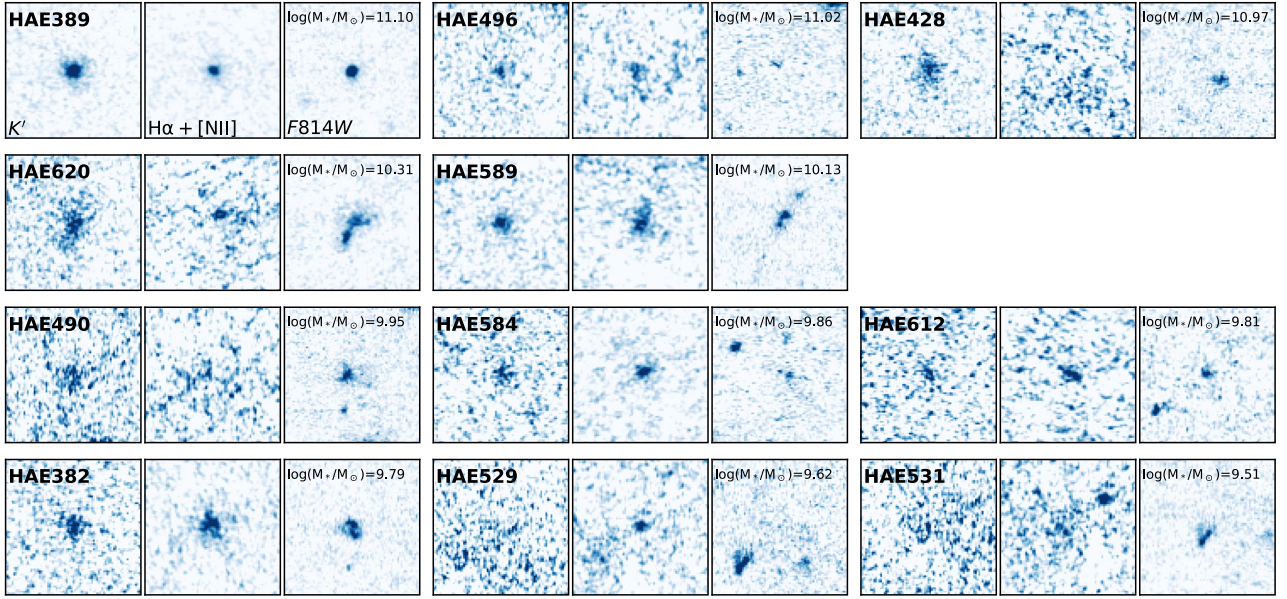


Fig. 2. IRCS/ K' , IRCS/ $NB2315 - K'$, and ACS/ I_{F814W} images for 11 $H\alpha$ emitters in the densest group in USS1558 (the image size is $4.3 \times 4.3 \text{ arcsec}^2$). The K' and $NB2315 - K'$ images correspond to the stellar continuum and the $H\alpha + [N II]$ emission line, respectively. The I_{F814W} images correspond to the rest-frame 2300 Å at $z \sim 2.53$. The IRCS + AO188 images have a similar resolution as HST. The top two rows show the $H\alpha$ emitters with $10.0 \leq \log(M_*/M_\odot) \leq 11.1$ (high-mass sub-sample). The bottom two rows show the $H\alpha$ emitters with $9.5 \leq \log(M_*/M_\odot) < 10.0$ (low-mass sub-sample). IDs are extracted from the catalog by Hayashi et al. (2016), and stellar masses are estimated by Shimakawa et al. (2018). (Color online)

Telescope/the Advanced Camera for Surveys (HST/ACS; subsection 3.3) for 11 $H\alpha$ emitters.

3.2 Stacking analysis

Unfortunately, the S/N of the obtained images are insufficient to investigate the resolved structures for the individual $H\alpha$ emitters. We decide to conduct stacking analyses to achieve higher S/N , and to discuss the average properties of their structures. We divide our 11 $H\alpha$ emitters into two sub-samples according to their stellar masses, namely a “high-mass sub-sample” including five $H\alpha$ emitters with $10 \leq \log(M_*/M_\odot) \leq 11.1$ and a “low-mass sub-sample” including six $H\alpha$ emitters with $9.5 \leq \log(M_*/M_\odot) < 10$.

Before stacking, we subtract the local sky for the individual targets because the local sky background is not completely subtracted in the pipeline. The local sky counts are estimated by taking an average of the counts at $r = 30\text{--}50$ pixel from the center of each target. Subsequently, we make cumulative radial profiles with a circular aperture, and determine total flux densities of the K' -band and $NB2315$ by taking an average of the cumulative values among radii where the profile is flat within a 1σ error range. Total continuum flux densities (f_c) are obtained from the K' -band images. The total fluxes of $H\alpha + [N II]$ line are estimated with the following equation:

$$F_{\text{line}} = \Delta_{NB} (f_{NB} - f_c), \quad (1)$$

where f_{NB} is a total flux density of $NB2315$ and Δ_{NB} is the FWHM of $NB2315$ filter ($0.03 \mu\text{m}$). After normalizing K' -band and $NB-K'$ images with total f_c and F_{line} , we conduct the median stacking with the IRAF/IMCOMBINE task. The central position of each target is determined as the flux-weighted center of the K' -band image.

The obtained stacked images are scaled to the median values of the continuum flux densities and the observed $H\alpha$ emission line fluxes measured with the MOIRCS images (Hayashi et al. 2016; Shimakawa et al. 2018). The stacked images of emission line maps are contributed from the $[N II]$ emission line because FWHM of the $NB2315$ filter covers both $H\alpha$ emission and $[N II]$ emission lines at $z = 2.53$. Scaling the stacked $NB-K'$ images to the median $H\alpha$ fluxes corresponds to assuming a constant $[N II]/H\alpha$ ratio across a galaxy. According to Macuga et al. (2019), in which a deep X-ray observation with Chandra was conducted ($L_X > 2 \times 10^{43} \text{ erg s}^{-1}$), none of our targets are detected in the X-ray. Our sample includes no X-ray active galactic nuclei (AGNs). Moreover, half of our targets were observed in previous NIR spectroscopic observations (Shimakawa et al. 2015a, 2015b), and the emission line widths in the obtained spectra indicate that they are unlikely host AGNs. When a galaxy does not host an AGN, the gradient of $[N II]/H\alpha$ can be regarded as the metallicity gradient. Considering that the metallicity gradient of star-forming galaxies at $z \gtrsim 1$ becomes flatter on average than local ones (e.g., Wuyts et al. 2016; Maiolino & Mannucci 2019), an

assumption of a constant $[N\text{ II}]/H\alpha$ ratio for our targets at $z = 2.53$ seems to be reasonable.

We note that the total flux densities obtained from the cumulative profiles for the individual targets are not necessarily consistent with those measured in MOIRCS images (K_s and $NB2315$). The former total flux densities tend to be lower than the later ones. Our IRCS + AO188 images seem to lose some fluxes because the image depths are insufficient to detect extended components especially for the faint $H\alpha$ emitters. We explain more details about this flux loss problem in the appendix. In the following sections, we do not take the missed fluxes into account, and we consider that the missed fluxes do not significantly affect our results obtained from the stacking analyses.

3.3 The rest-frame UV images of the HST

Imaging observations by HST/ACS for USS1558 were conducted in 2014 July (GO-13291; PI: M. Hayashi). The I_{F814W} -band images, which correspond to the rest-frame $\sim 2300\text{ \AA}$ at $z = 2.53$, are available for all the IRCS targets (figure 2). The 3σ limiting magnitude is 28.7 mag with a $0''.2$ diameter aperture after correcting for the Galactic extinction of 0.3 mag (Schlegel et al. 1998). We match the PSF of the HST image to that of the IRCS K' -band image as conducted in subsection 3.1. Subsequently, the smoothed images of the individual $H\alpha$ emitters are stacked in the same manner as for the IRCS images. The central position of each target is determined with the K' -band image. The stacked images are scaled to the median flux densities of the I_{F814W} -band. We use the rest-frame UV images to estimate $A_{H\alpha}$ as a function of distance from the center (subsection 4.1).

4 Results and discussion

4.1 Radially dependent dust extinction of $H\alpha$

We estimate $A_{H\alpha}$ as a function of radius using the stacked $H\alpha$ images and the stacked I_{F814W} -band images (subsection 3.3). Koyama et al. (2015) established an empirical relation using local star-forming galaxies from SDSS to estimate $A_{H\alpha}$:

$$A_{H\alpha} = (0.101 \times \log EW_{H\alpha} + 0.872) \times \log(H\alpha/UV) + (-0.776 \times \log EW_{H\alpha} + 1.688), \quad (2)$$

where $\log EW_{H\alpha}$ is the EW of the $H\alpha$ emission line in the rest-frame, and $\log(H\alpha/UV)$ is a ratio between the observed SFR obtained from $H\alpha$ and that from UV with Kroupa IMF (Kroupa 2002) [equations (9)–(11) in Koyama et al. (2015)].

We divide the radial profiles of the $H\alpha$ flux by those of the continuum flux density to obtain the radial profiles

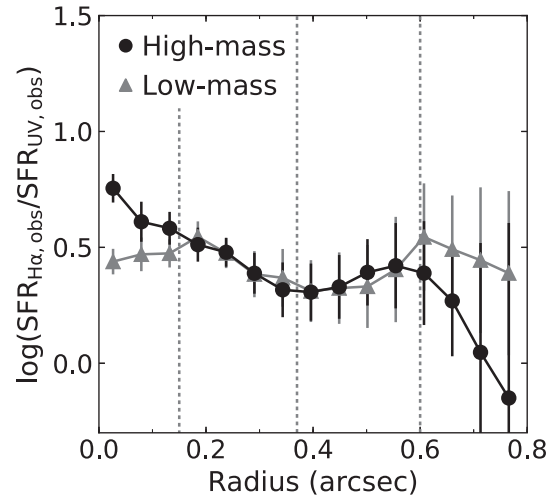


Fig. 3. Radial profiles of the ratio between $SFR_{H\alpha, \text{obs}}$ and $SFR_{UV, \text{obs}}$ for the two sub-samples. At the central region of the high-mass sub-sample, $SFR_{H\alpha, \text{obs}}/SFR_{UV, \text{obs}}$ becomes higher compared to that of the outer parts. As for the low-mass sub-sample, the SFR ratio is almost flat. The vertical dotted lines correspond to the radii, where we take an average of the SFR ratios. The SFR ratios have large uncertainties at $r > 0''.6$.

of $EW_{H\alpha}$. The radial profiles of $SFR_{H\alpha}$ are then obtained from those of $F_{H\alpha, \text{obs}}$ with the Kennicutt (1998) relation. As for the profiles of $SFR_{UV, \text{obs}}$, we converted the I_{F814W} flux densities ($\sim 2300\text{ \AA}$ in the rest-frame) to SFRs with the Kennicutt (1998) relation, although Koyama et al. (2015) used far-UV data rather than near-UV data. Figure 3 shows radial profiles of the ratio between $SFR_{H\alpha, \text{obs}}$ and $SFR_{UV, \text{obs}}$ for the two sub-samples. The observed SFR ratio seems to increase toward the central region for the high-mass sub-sample, whereas the low-mass sub-sample shows almost a flat profile.

When estimating $A_{H\alpha}$ with equation (2), we divide the radial profile into three bins, namely, $r \leq 0''.15$, $0''.15 < r < 0''.37$, and $0''.37 \leq r \leq 0''.6$, to achieve higher S/N. Because the observed SFR ratios and $EW_{H\alpha}$ have large uncertainties at $r > 0''.6$, we assume that $A_{H\alpha}$ is constant at $r > 0''.6$, and use $A_{H\alpha}$ at $0.37 \leq r \leq 0.6$. The obtained $A_{H\alpha}$ in each radial bin are as follows: $A_{H\alpha} = 1.11, 0.77$, and 0.67 mag for the high-mass sub-sample; and $A_{H\alpha} = 0.51, 0.46$, and 0.40 mag for the low-mass sub-sample. Uncertainties in $A_{H\alpha}$ are 0.05 – 0.1 mag. As expected from figure 3, the central region of the high-mass sub-sample has stronger dust extinction, and the low-mass sub-sample has a nearly constant $A_{H\alpha}$. The obtained trend is consistent with results of previous studies, such as Nelson et al. (2016a) and Tacchella et al. (2018), although their results show higher $A_{H\alpha}$, for example, $A_{H\alpha} \gtrsim 2$ mag at $r < 1$ kpc.

We confirm that how to divide the radial profiles with radii has little impact on the final dust-extinction-corrected radial profiles in subsection 4.2. Furthermore, as a test,

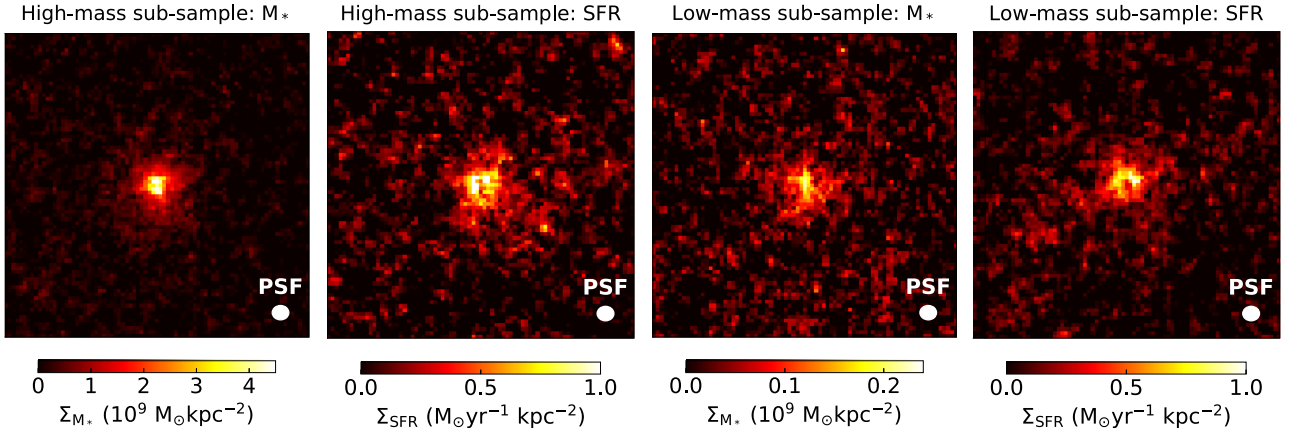


Fig. 4. Stacked images of the stellar mass and $\text{SFR}_{\text{H}\alpha, \text{corr}}$ for the two sub-samples with the radially dependent $A_{\text{H}\alpha}$ (subsection 4.1). The box size of each panel is $\sim 4.3 \times 4.3 \text{ arcsec}^2$. The small white circle in each panel shows the PSF size (FWHM). (Color online)

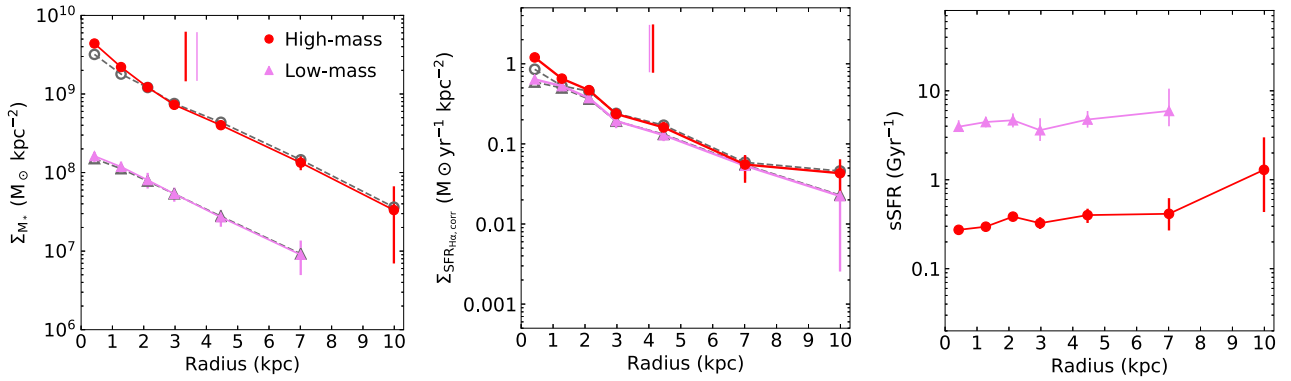


Fig. 5. Radial profiles of the two sub-samples. From the left to right, each panel shows the radial profiles of stellar mass surface density, those of SFR surface density, and those of sSFR. In the left-hand and the middle panels, the filled symbols represent the results using the radially dependent $A_{\text{H}\alpha}$ (subsection 4.1). The open symbols represent the results with the uniform $A_{\text{H}\alpha}$. The vertical lines in the left-hand and middle panels represent $R_{1/2}$ for the stellar component and star-forming region with the radially dependent $A_{\text{H}\alpha}$. The thick ones show $R_{1/2}$ for the high-mass sub-sample. The SFR profiles of the two sub-samples have a flatter slope than the stellar mass profiles. (Color online)

we estimate total $A_{\text{H}\alpha}$ for the two sub-samples using the median values of $F_{\text{H}\alpha}$, f_c , and $\text{SFR}_{\text{UV, obs}}$. The total $A_{\text{H}\alpha}$ is estimated to be 0.65 mag and 0.40 mag for the high-mass and low-mass sub-samples, respectively. The total values are close to those at $0''.37 \leq r \leq 0''.6$, indicating that our $A_{\text{H}\alpha}$ measurement for the spatially resolved maps is reasonable.

We note that equation (2) is calibrated with the local star-forming galaxies at $\text{EW}_{\text{H}\alpha} < 100 \text{ \AA}$, whereas the low-mass sub-sample has a median EW of $\sim 160 \text{ \AA}$. We extrapolate equation (2) toward a slightly higher EW for the low-mass sub-sample. Additionally, it is unclear whether the locally calibrated equation is applicable for star-forming galaxies at $z = 2.53$, because a typical $\text{EW}_{\text{H}\alpha}$ at a fixed stellar mass changes with redshift (Sobral et al. 2014). Although we must keep these facts in mind, the methods of estimating the radial dependence of $A_{\text{H}\alpha}$ with the currently available data are quite limited. Ideally, we would need spatially

resolved Balmer decrement ($\text{H}\alpha/\text{H}\beta$ ratio) maps to estimate $A_{\text{H}\alpha}$ more accurately, as conducted in Nelson et al. (2016a).

4.2 Stacked stellar mass/SFR maps and radial profiles

Figure 4 shows the stacked images of the stellar mass and dust-extinction-corrected $\text{SFR}_{\text{H}\alpha}$ for the two sub-samples. The stacked images of f_c (subsection 3.2) are corrected for the dust extinction using radially dependent $A_{\text{H}\alpha}$ (subsection 4.1). Here we assume no extra extinction for the $\text{H}\alpha$ emission line compared to the extinction for stellar components, i.e., $f = 1$ (e.g., Erb et al. 2006; Reddy et al. 2010, 2015). Subsequently, the image of the intrinsic f_c for each sub-sample is converted to the stellar mass image by multiplying a constant $M_*/f_{c, \text{int}}$ ratio, where $f_{c, \text{int}}$ is the total continuum flux density measured from the cumulative

profile of the dust-extinction-corrected f_c image. Multiplying a constant $M_*/f_{c,\text{int}}$ corresponds to assuming a constant intrinsic mass-to-light ratio (M_*/L_{int}) across a galaxy. Because M/L depends not only on dust extinction but also on age, some of our targets can have radial gradients of M_*/f_c even after the radially dependent dust extinction correction is applied. As for the dust-extinction-corrected $\text{SFR}_{\text{H}\alpha}$ images, we convert the stacked images of $F_{\text{H}\alpha}$ obtained in subsection 3.2 to those of $\text{SFR}_{\text{H}\alpha}$ with radially dependent $A_{\text{H}\alpha}$ and the Kennicutt (1998) relation. We then determine the total SFRs for the two sub-samples from cumulative profiles of the $\text{SFR}_{\text{H}\alpha, \text{corr}}$ images.

For a fair comparison with the field galaxies in subsection 4.3, we also create the images of stellar mass and $\text{SFR}_{\text{H}\alpha, \text{corr}}$ with radially constant $A_{\text{H}\alpha}$. In this case, we just scale the observed f_c and $F_{\text{H}\alpha}$ images so that the total stellar mass and SFR are matched to those derived from the images with radially dependent $A_{\text{H}\alpha}$.

Figure 5 shows radial profiles of the stellar mass surface density, SFR surface density, and specific SFR (sSFR) for the two sub-samples. Radial profiles of the stellar mass and SFR surface density are obtained by taking an average in an azimuth direction with a circular aperture. The sSFR profile is obtained by dividing the SFR surface density profile by the stellar mass surface density profile. Two kinds of radial profiles are shown for each sub-sample in the left-hand and middle panels of figure 5, which represent the two results using different dust extinction corrections. Comparing the radial profiles of the stellar surface density and SFR surface density, we find that the SFR profile becomes flatter than the stellar mass profile at $r \gtrsim 2\text{--}3$ kpc for the two sub-samples.

4.3 Size comparison between star-forming regions and stellar components

Table 2 summarizes sizes ($R_{1/2}$) of the stellar mass and $\text{SFR}_{\text{H}\alpha, \text{corr}}$ distributions for the two sub-samples. $R_{1/2}$ is defined as the radius where the cumulative value becomes a half of the total M_* or $\text{SFR}_{\text{H}\alpha, \text{corr}}$. Error bars on $R_{1/2}$ represent the 1σ scatter of the cumulative values from the total

value at the outer regions where a change of the cumulative value is comparable to or less than a noise level.

We show the two $R_{1/2}$ of M_* and $\text{SFR}_{\text{H}\alpha, \text{corr}}$ with different assumptions for dust extinction correction. The $R_{1/2}$ with the radially dependent $A_{\text{H}\alpha}$ becomes smaller than that with the uniform $A_{\text{H}\alpha}$ for the high-mass sub-sample as expected from the strong dust extinction at the center in the former case (figure 5). Regardless of the dust extinction correction methods, the size measured in the SFR map is larger than that measured in the stellar mass map for the high-mass sub-sample, which indicates that the star-forming region is more extended than the underlying stellar component. Such a further extended star-forming region can also be seen in the comparison of the two radial profiles as mentioned in subsection 4.2. As for the low-mass sub-sample, the $R_{1/2}$ values of the two components are the same within 1σ error bars (table 2).

We compare the sizes measured with the method mentioned above and IRCS K' -band images and those measured with GALFIT and HST/WFC3 H_{F160W} -band images (Shimakawa et al. 2018). Here we use the stacked images and the individual images of the bright targets. As a result, we find that our measurement shows systematically larger sizes by a factor of ~ 1.8 compared to the measurement with GALFIT. Such a systematic difference may be due to the fact that our measurement does not deconvolve a PSF and does not use a Sérsic profile to fit the images. We note, however, that the relative comparison remains valid as long as we use sizes measured with the same method.

4.4 Environmental dependence of mass-size relation

In figure 6, we compare $R_{1/2}$ measured in the stacked images between our sample and the sample of the field galaxies at $z = 2\text{--}2.5$ in Minowa et al. (2019). Their sample consists of 20 H α emitters at $z = 2.18, 2.23$, and 2.53 in the UDS and COSMOS field (Tadaki et al. 2013; Sobral et al. 2013), which cover a stellar mass range of $\log(M_*/M_\odot) \sim 9\text{--}11$. The field sample distributes around the star-forming main sequence at the epoch. The same methods are used for stacking and also measuring $R_{1/2}$. One difference is that

Table 2. Summary of the total stellar mass, dust-extinction-corrected total SFRs, and sizes of the stellar components and star-forming regions for the two sub-samples in USS1558.

	Total		Radially dependent $A_{\text{H}\alpha}$		Uniform $A_{\text{H}\alpha}$	
	Stellar mass $\log(M_*/M_\odot)$	$\text{SFR}_{\text{H}\alpha, \text{corr}}$ ($M_\odot \text{ yr}^{-1}$)	$R_{1/2}(M_*)$ (kpc)	$R_{1/2}(\text{SFR}_{\text{H}\alpha, \text{corr}})$ (kpc)	$R_{1/2}(M_*)$ (kpc)	$R_{1/2}(\text{SFR}_{\text{H}\alpha, \text{corr}})$ (kpc)
High mass	10.97	37.77	$3.34^{+0.16}_{-0.15}$	4.13 ± 0.11	3.65 ± 0.16	4.37 ± 0.13
Low mass	9.80	28.23	$3.70^{+0.45}_{-0.39}$	4.02 ± 0.23	$3.77^{+0.46}_{-0.39}$	$4.12^{+0.24}_{-0.23}$

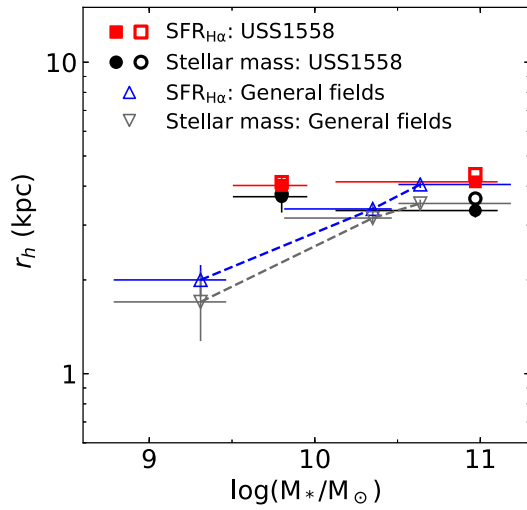


Fig. 6. Relation between the total stellar mass and size of the stellar components and star-forming regions for the $H\alpha$ emitters in different density fields at $z = 2-2.5$. Sizes measured in the stacked images are shown for the two samples. The filled symbols represent $R_{1/2}$ assuming the radially dependent $A_{H\alpha}$, whereas the open symbols represent $R_{1/2}$ obtained with the uniform $A_{H\alpha}$. Both in the general fields and in the proto-cluster core, star-forming regions are more extended than the underlying stellar components at least for the massive star-forming galaxies with $\log(M_*/M_\odot) \sim 10-11$. (Color online)

uniform $A_{H\alpha}$ is assumed for the field galaxies. In figure 6, we show the two $R_{1/2}$ with different assumptions in $A_{H\alpha}$ for USS1558 sub-samples. We should look at $R_{1/2}$ with the same $A_{H\alpha}$ recipe for a fair comparison with the results of the field galaxies.

At least at $\log(M_*/M_\odot) \geq 10$, the star-forming galaxies in the different environments at $z = 2-2.5$ have similar sizes for each component and show the same trend; that the star-forming region is more extended than the underlying stellar component [Nelson et al. (2016b) for $z \sim 1$ star-forming galaxies in general fields]. Massive star-forming galaxies at $z = 2-2.5$ seem to build up their structures from inside to outside in spite of their surrounding environments.

As for the low-mass sub-sample, the sizes of the stellar mass and SFR are marginally larger than those for the field counterparts. We find no clear dependence of $R_{1/2}$ on stellar mass for the two sub-samples in USS1558, in contrast to the field sub-samples. Shimakawa et al. (2018) also reported little correlation between stellar mass and size for the $H\alpha$ emitters in USS1558 using the HST/ H_{160W} -band images and GALFIT. A weak dependence of $R_{1/2}$ on stellar mass in our IRCS targets may be partly due to systematically higher sSFRs for the low-mass sub-sample (figure 1, subsection 2.1). Indeed, some studies reported a weak positive correlation between sSFRs (or the deviation from the star-forming main sequence) and sizes of star-forming galaxies (e.g., Wuyts et al. 2011; Whitaker et al. 2017; Socolovsky et al. 2019).

4.5 Structural evolution by star formation in the proto-cluster environment

In this subsection, we discuss the subsequent evolution of the total stellar mass and the stellar mass surface density at $r < 1$ kpc (Σ_1) by continued star formation for the two sub-samples in USS1558.

Barro et al. (2017) suggested that star-forming galaxies in a normal star formation phase and those in a compaction phase follow different evolutionary tracks on the $\log(M_*)$ – $\log(\Sigma_1)$ diagram. When star-forming galaxies evolve in the inside-out manner, they likely move on this diagram along the relation of $\log \Sigma_1 \propto 0.9 \log M_*$. When galaxies are in a compaction phase, in which bulge-like structures are rapidly built up at the center, their evolutionary track becomes steeper than that of the inside-out growth, namely, $\log \Sigma_1 \propto 1.3 \log M_*$, to move the sequence of quiescent populations.

Assuming a constant SFR with time, we calculate how the total stellar mass and Σ_1 changes using the total $SFR_{H\alpha, \text{corr}}$ and Σ_{SFR} at $r < 1$ kpc. We calculate $\Delta \log \Sigma_1 / \Delta \log M_*$ with $\Delta t = 500$ Myr as an example case. As a result, we obtain $\Delta \log \Sigma_1 / \Delta \log M_* = 0.68$ for the high-mass sub-sample and 0.95 for the low-mass sub-sample. The results do not depend on Δt . The low-mass sub-sample seems to increase the central mass surface density and total stellar mass along the evolutionary path of galaxies in a normal star formation phase with $\Delta \log \Sigma_1 / \Delta \log M_* = 0.9-1.0$ (Tacchella et al. 2016; Barro et al. 2017). As for the high-mass sub-sample, the central mass surface density seems to grow more slowly than the total stellar mass, and the values of $\Delta \log \Sigma_1 / \Delta \log M_*$ are close to the slope of the $\log M_*$ – $\log \Sigma_1$ relation for quiescent galaxies (Fang et al. 2013; Barro et al. 2017). Such a flatter evolutionary path is suggested in the simulations for galaxies in the inside-out quenching phase after the compaction event (Zolotov et al. 2015; Tacchella et al. 2016). However, the sSFR profile of the high-mass sub-sample shows a weak decline toward the center rather than a strong suppression at the center (the right-hand panel of figure 5). Considering compact dust emission observed at the center of massive star-forming galaxies at high redshifts (e.g., Barro et al. 2016; Tadaki et al. 2017), the shallower slope of the high-mass sub-sample may be explained by dust-obscured star formation which cannot be fully recovered in our method with UV and $H\alpha$.

The obtained results shown in subsections 4.2 and 4.3 and $\Delta \log \Sigma_1 / \Delta \log M_*$ values suggest that our samples in the dense proto-cluster core have an extended star-forming disk and evolve their structures in a secular way from inside to outside. We find no clear sign of the ongoing compaction event in the stacked SFR or sSFR profiles, implying that gas-rich mergers or violent disk instabilities may be

sub-dominant processes on average in the high-density region at $z \sim 2.5$. In Shimakawa et al. (2017, 2018), it was reported that star-forming galaxies in the dense groups in USS 1558 have systematically higher sSFRs than those in the less-dense regions and that such high star-forming activity may be supported by a large amount of H I gas residing in the proto-cluster core. Our results on the spatial extent of the star-forming region within the galaxies in the densest group suggest that their star-forming activity is enhanced across the entire disk rather than concentrated only at the central region (Nelson et al. 2016b). Their extended star-forming disks may be maintained by continuous, steady gas inflow from outside (e.g., Davé et al. 2011) keeping its angular momentum.

Our results also indicate that gas removal processes, such as ram pressure stripping, may not be acting on star-forming galaxies effectively in the proto-cluster core at $z = 2.53$, in contrast to local high-density environments where star-forming galaxies tend to show truncated star-forming disks (e.g., Koopmann and Kenney 2004; Schaefer et al. 2019). Because the proto-cluster is in a vigorous assembly phase and the potential well is likely still immature as compared to the local clusters (Chiang et al. 2017), interactions with hot gas in the cluster core may not be active yet.

Note that we show only the average trends among our sample based on the stacking analyses. We might observe a centrally concentrated star-forming region for some of our targets if we look at the individual galaxies. Investigating the internal distribution of star-forming regions in the individual galaxies is necessary to evaluate the relative contributions among different physical processes and their environmental dependence. Moreover, considering a high fraction of low-mass [$\log(M_*/M_\odot) \lesssim 9$] galaxies with elevated SFRs in this proto-cluster field (Hayashi et al. 2016), such low-mass galaxies may hold key information on the early environmental dependence. Investigation of internal structures in those low-mass systems must therefore be very important, although such studies require much deeper imaging data.

5 Summary

We conducted the AO-assisted K' -band and NB imaging observations with Subaru/IRCS + AO188 for the star-forming galaxies in the dense proto-cluster core at $z = 2.53$. By combining AO and the NB filter, we were able to resolve the H α -emitting regions within the galaxies spatially. We obtained the images for 11 H α emitters with an angular resolution (FWHM) of $0''.25$, corresponding to 2 kpc at $z = 2.53$.

We conducted the stacking analyses by dividing the sample into two stellar mass bins, namely, the high-mass

sub-sample with $\log(M_*/M_\odot) = 10.0$ – 11.1 and the low-mass sub-sample with $\log(M_*/M_\odot) = 9.5$ – 10.0 . With the stacked images, we compared the spatial distribution of star-forming regions and the underlying stellar components. Our findings are the following:

- The sizes of the stellar components are estimated to be $R_{1/2} = 3.34^{+0.16}_{-0.15}$ kpc and $3.70^{+0.45}_{-0.39}$ kpc for the high-mass and low-mass sub-sample, respectively, when assuming the radially dependent dust extinction for H α . The sizes of the star-forming regions traced by H α are estimated to be $R_{1/2} = 4.13 \pm 0.11$ kpc and 4.02 ± 0.23 kpc for the high-mass and low-mass sub-sample. The high-mass sub-sample shows a more extended star forming-region than the underlying stellar component.
- Comparing our results for the proto-cluster with those for the field galaxies at $z = 2$ – 2.5 on the stellar mass– $R_{1/2}$ diagram, we found no clear environmental dependence at least for relatively massive galaxies. They have more extended star-forming regions than stellar components irrespective of the environments. Our low-mass sub-sample in the proto-cluster has slightly larger $R_{1/2}$ than the field counterparts, but this may be in part related to systematically high sSFRs for the low-mass sub-sample in USS1558.
- We investigated the growth of the total stellar mass and central mass surface density at $r < 1$ kpc by assuming a constant SFR during a given time period. The high-mass and low-mass sub-samples show $\Delta \log(\Sigma_1)/\Delta \log(M_*) \sim 0.68$ and 0.95 , respectively. These values indicate that the two sub-samples likely grow their structures in an inside-out manner rather than by a compaction event (Barro et al. 2017).

Our results suggest that the structural growth of star-forming galaxies at $z = 2$ – 2.5 is dominated by internal secular processes even in the dense proto-cluster core, and that galaxies at least with $\log(M_*/M_\odot) \geq 9.5$ are forming stars over their entire disks.

Deep AO-assisted IFU observations to detect multiple emission lines will enable us to investigate radial profiles of [N II]/H α and H α /H β ratios for more accurate estimations of SFR distributions. Additionally, tracing the dust emission distribution by rest-frame infrared observations is also required to uncover the star formation activity that is largely obscured in the rest-frame UV-optical regime. The Atacama Large Millimeter/submillimeter Array (ALMA) will allow us to map such dusty star-forming regions with the same (or higher) angular resolution as that of the AO-assisted observations (e.g., Barro et al. 2016; Tadaki et al. 2017). Also, mapping molecular gas components within galaxies with ALMA will be crucial to investigating the presence of the compaction event more directly.

Acknowledgment

We thank the anonymous referee for careful reading and comments that improved the clarity of this paper. We would like to thank the Subaru telescope staff for supporting the observations. This work is based on observations made with the National Aeronautics and Space Administration/the European Space Agency Hubble Space Telescope, obtained at the Space Telescope Science Institute, which is operated by the Association of Universities for Research in Astronomy, Inc., under NASA contract NAS 5-26555. These observations are associated with program GO-13291. Data analyses were in part carried out on the open use data analysis computer system at the Astronomy Data Center, ADC, of the National Astronomical Observatory of Japan (NAOJ). A part of this study is conducted with the Tool for OPERations on Catalogues And Tables (TOPCAT; Taylor 2005). TK acknowledges support by the Japan Society for the Promotion of Science KAKENHI Grant Number JP18H03717.

Appendix. Comparison of total fluxes between IRCS and MOIRCS

Figure 7 shows a comparison of total flux densities between the IRCS K' -band/ $NB2315$ images (as mentioned in subsection 3.2) and the MOIRCS K_s -band/ $NB2315$ images (Hayashi et al. 2016) as a function of S/N of the flux densities of the IRCS images. The total fluxes for the MOIRCS images represent the Korn fluxes measured with SExtractor (Bertin & Arnouts 1996). The IRCS flux densities tend to be smaller than the MOIRCS flux densities at lower S/N , indicating that some fluxes are missed in our IRCS + AO188 imaging observations. This is probably caused by the lower throughput and higher thermal background of IRCS than MOIRCS. These factors lead to lower sensitivity of IRCS especially for diffuse components. As

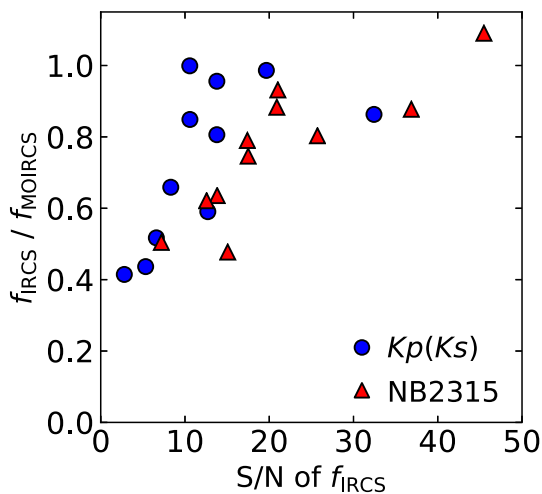


Fig. 7. Flux density ratio between IRCS (K' and $NB2315$) and MOIRCS (K_s and $NB2315$) as a function of S/N of the IRCS total flux density for 11 $H\alpha$ emitters analyzed in this study. The total flux density ratios become smaller with decreasing S/N , indicating that the extended components for the faint emitters tend to be missed in the IRCS + AO188 images. (Color online)

a result, the depths of the current data are insufficient to detect extended emission from the $H\alpha$ emitters.

The average value $f_{\text{IRCS}}/f_{\text{MOIRCS}}$ in the $K'_{(s)}$ -band ($NB2315$) image is 84(86)% for the high-mass sub-sample and 65(68)% for the low-mass sample. The missed fluxes are less than 20% for most objects in the high-mass sub-sample. We consider that the missed fluxes do not strongly affect our results obtained from the stacking analyses for the high-mass sub-sample. As for the low-mass sub-sample, flux loss may lead to underestimation of size. However, when comparing the size of the stacked K' -band image with that measured from the stacked H_{F160W} -band image with GALFIT (subsection 4.3), the size in our measurement is rather larger than the GALFIT result. We unlikely underestimate the size due to the flux loss, and the systematic offset in our size measurement seems to affect the result dominantly.

References

- Allen, R. J., et al. 2017, *ApJ*, 834, L11
- Barro, G., et al. 2016, *ApJ*, 827, L32
- Barro, G., et al. 2017, *ApJ*, 840, 47
- Belfiore, F., et al. 2018, *MNRAS*, 477, 3014
- Bertin, E., & Arnouts, S. 1996, *A&AS*, 117, 393
- Best, P., et al. 2013, in *Thirty Years of Astronomical Discovery with UKIRT*, ed. A. Adamson et al. (Dordrecht: Springer), 235
- Chabrier, G. 2003, *PASP*, 115, 763
- Chiang, Y.-K., Overzier, R. A., Gebhardt, K., & Henriques, B. 2017, *ApJ*, 844, L23
- Daddi, E., et al. 2007, *ApJ*, 670, 156
- Davé, R., Oppenheimer, B. D., & Finlator, K. 2011, *MNRAS*, 415, 11
- Dekel, A., & Birnboim, Y. 2006, *MNRAS*, 368, 2
- Dekel, A., & Burkert, A. 2014, *MNRAS*, 438, 1870
- Ellison, S. L., Sánchez, S. F., Ibarra-Medel, H., Antonio, B., Mendel, J. T., & Barrera-Ballesteros, J. 2018, *MNRAS*, 474, 2039
- Erb, D. K., Steidel, C. C., Shapley, A. E., Pettini, M., Reddy, N. A., & Adelberger, K. L. 2006, *ApJ*, 647, 128
- Fang, J. J., Faber, S. M., Koo, D. C., & Dekel, A. 2013, *ApJ*, 776, 63
- Förster Schreiber, N. M., et al. 2009, *ApJ*, 706, 1364
- Förster Schreiber, N. M., et al. 2018, *ApJS*, 238, 21
- Franx, M., van Dokkum, P. G., Förster Schreiber, N. M., Wuyts, S., Labbé, I., & Toft, S. 2008, *ApJ*, 688, 770
- Gobat, R., et al. 2013, *ApJ*, 776, 9
- Gunn, J. E., & Gott, J. R., III 1972, *ApJ*, 176, 1
- Hayano, F., Kawai, A., Uchikawa, T., Endo, K., Yoshino, K., Yamazaki, Y., Nagashima, K., & Tsuchiya, K. 2010, *SPIE Proc.*, 7638, 76380E
- Hayano, Y., et al. 2008, *SPIE Proc.*, 7015, 701510
- Hayashi, M., Kodama, T., Tadaki, K., Koyama, Y., & Tanaka, I. 2012, *ApJ*, 757, 15
- Hayashi, M., Kodama, T., Tanaka, I., Shimakawa, R., Koyama, Y., Tadaki, K., Suzuki, T. L., & Yamamoto, M. 2016, *ApJ*, 826, L28
- Hine, N. K., et al. 2016, *MNRAS*, 460, 4075

- Ichikawa, T., et al. 2006, SPIE Proc., 6269, 626916
- Kajisawa, M., Kodama, T., Tanaka, I., Yamada, T., & Bower, R. 2006, MNRAS, 371, 577
- Kashino, D., et al. 2013, ApJ, 777, L8
- Kato, Y., et al. 2016, MNRAS, 460, 3861
- Kennicutt, R. C., Jr. 1998, ARA&A, 36, 189
- Kereš, D., Katz, N., Fardal, M., Davé, R., & Weinberg, D. H. 2009, MNRAS, 395, 160
- Kereš, D., Katz, N., Weinberg, D. H., & Davé, R. 2005, MNRAS, 363, 2
- Kobayashi, N., et al. 2000, SPIE Proc., 4008, 1056
- Kodama, T., Hayashi, M., Koyama, Y., Tadaki, K., Tanaka, I., & Shimakawa, R. 2013, IAU Symp. 295, The Intriguing Life of Massive Galaxies, ed. D. Thomas et al. (Cambridge: Cambridge University Press), 74
- Koopmann, R. A., & Kenney, J. D. P. 2004, ApJ, 613, 866
- Koyama, Y., et al. 2015, MNRAS, 453, 879
- Koyama, Y., Kodama, T., Tadaki, K., Hayashi, M., Tanaka, M., Smail, I., Tanaka, I., & Kurk, J. 2013, MNRAS, 428, 1551
- Kroupa, P. 2002, Science, 295, 82
- Kubo, M., Yamada, T., Ichikawa, T., Kajisawa, M., Matsuda, Y., Tanaka, I., & Umehata, H. 2017, MNRAS, 469, 2235
- Law, D. R., Steidel, C. C., Erb, D. K., Larkin, J. E., Pettini, M., Shapley, A. E., & Wright, S. A. 2009, ApJ, 697, 2057
- Law, D. R., Steidel, C. C., Erb, D. K., Pettini, M., Reddy, N. A., Shapley, A. E., Adelberger, K. L., & Simenc, D. J. 2007, ApJ, 656, 1
- Lotz, J. M., et al. 2013, ApJ, 773, 154
- Macuga, M., et al. 2019, ApJ, 874, 54
- Maiolino, R., & Mannucci, F. 2019, A&AR, 27, 3
- Matharu, J., et al. 2019, MNRAS, 484, 595
- Mihos, J. C., & Hernquist, L. 1996, ApJ, 464, 641
- Minowa, Y., et al. 2005, ApJ, 629, 29
- Minowa, Y., et al. 2012, SPIE Proc., 8447, 84471F
- Minowa, Y., et al. 2019, PASJ, submitted
- Nelson, E. J., et al. 2016a, ApJ, 817, L9
- Nelson, E. J., et al. 2016b, ApJ, 828, 27
- Noeske, K. G., et al. 2007, ApJ, 660, L43
- Noguchi, M. 1999, ApJ, 514, 77
- Overzier, R. A. 2016, A&AR, 24, 14
- Overzier, R. A., et al. 2008, ApJ, 673, 143
- Peng, C. Y., Ho, L. C., Impey, C. D., & Rix, H.-W. 2010, AJ, 139, 2097
- Peter, A. H. G., Shapley, A. E., Law, D. R., Steidel, C. C., Erb, D. K., Reddy, N. A., & Pettini, M. 2007, ApJ, 668, 23
- Reddy, N. A., et al. 2015, ApJ, 806, 259
- Reddy, N. A., Erb, D. K., Pettini, M., Steidel, C. C., & Shapley, A. E. 2010, ApJ, 712, 1070
- Salpeter, E. E. 1955, ApJ, 121, 161
- Schaefer, A. L., et al. 2019, MNRAS, 483, 2851
- Schlegel, D. J., Finkbeiner, D. P., & Davis, M. 1998, ApJ, 500, 525
- Shibuya, T., Ouchi, M., & Harikane, Y. 2015, ApJS, 219, 15
- Shimakawa, R., et al. 2015a, MNRAS, 451, 1284
- Shimakawa, R., et al. 2017, MNRAS, 468, L21
- Shimakawa, R., et al. 2018, MNRAS, 473, 1977
- Shimakawa, R., Kodama, T., Tadaki, K., Hayashi, M., Koyama, Y., & Tanaka, I. 2015b, MNRAS, 448, 666
- Sobral, D., Best, P. N., Matsuda, Y., Smail, I., Geach, J. E., & Cirasuolo, M. 2012, MNRAS, 420, 1926
- Sobral, D., Best, P. N., Smail, I., Mobasher, B., Stott, J., & Nisbet, D. 2014, MNRAS, 437, 3516
- Sobral, D., Smail, I., Best, P. N., Geach, J. E., Matsuda, Y., Stott, J. P., Cirasuolo, M., & Kurk, J. 2013, MNRAS, 428, 1128
- Socolovsky, M., Maltby, D. T., Hatch, N. A., Almaini, O., Wild, V., Hartley, W. G., Simpson, C., & Rowlands, K. 2019, MNRAS, 482, 1640
- Swinbank, A. M., Sobral, D., Smail, I., Geach, J. E., Best, P. N., McCarthy, I. G., Crain, R. A., & Theuns, T. 2012, MNRAS, 426, 935
- Tacchella, S., et al. 2018, ApJ, 859, 56
- Tacchella, S., Dekel, A., Carollo, C. M., Ceverino, D., DeGraf, C., Lapiner, S., Mandelker, N., & Primack, J. R. 2016, MNRAS, 457, 2790
- Tadaki, K., et al. 2017, ApJ, 834, 135
- Tadaki, K., Kodama, T., Tanaka, I., Hayashi, M., Koyama, Y., & Shimakawa, R. 2013, ApJ, 778, 114
- Tadaki, K., Kodama, T., Tanaka, I., Hayashi, M., Koyama, Y., & Shimakawa, R. 2014, ApJ, 780, 77
- Taylor, M. B. 2005, ASP Conf. Ser., 347, 29
- Tokunaga, A. T., et al. 1998, SPIE Proc., 3354, 512
- Tomczak, A. R., et al. 2016, ApJ, 817, 118
- Trujillo, I., et al. 2006, ApJ, 650, 18
- van der Wel, A., et al. 2014, ApJ, 788, 28
- Venemans, B. P., et al. 2007, A&A, 461, 823
- Wang, T., et al. 2016, ApJ, 828, 56
- Whitaker, K. E., et al. 2017, ApJ, 838, 19
- Wuyts, E., et al. 2016, ApJ, 827, 74
- Wuyts, S., et al. 2011, ApJ, 742, 96
- Wuyts, S., et al. 2013, ApJ, 779, 135
- Zolotov, A., et al. 2015, MNRAS, 450, 2327